MP3D: Low-Cost 3D analysis of Microplastics with DFF

Victor Sim[1], Josiah Essiam[1], and Henry Ng[1]

Winchester College, College St, Winchester SO23 9NA

Abstract. Microplastics, formed by the breakdown of non-biodegradable plastic, pose a significant threat to aquatic ecosystems. To address this, accurate methods for quantifying microplastic concentrations are necessary for informing policy and prosecuting polluters. Current detection methods, however, require expensive equipment and are often unreliable. We propose a new, cost-effective methodology that leverages depth-from-focus methodologies to perform 3D analysis of microplastics. 3D analysis will provide more accurate measures of concentration than existing count-based methodologies. Additionally, qualitative analysis of the data can provide deeper insights into the physical and biological mechanisms behind microplastic-driven ecosystem damage.

1 Introduction

1.1 Problem Statement

Microplastic (defined as water-insoluble, solid polymer particles that are $\leq$5mm in size [5]) pollution has become an increasingly alarming issue. The number of microplastics in aquatic ecosystems is concerning: there are between 82 and 358 trillion microplastics in the world's oceans, weighing between 1.1 and 4.9 million tons. [7].

Microplastics (MP) have significant impacts on marine ecosystems. According to Lee et al [15], "Microplastics ... move easily through the food chain and persist in the environment". Ingestion of MPs results in "physical and mechanical harm to marine organisms", causing "abnormalities in internal organs" and malnutrition due to "microplastic accumulation". Even exposure to MPs can cause harm: MPs "attach to the surface of skin, crust and ectoderm" [4] of small marine organisms.

To combat this, we present a novel method for cost-effective and automated analysis of MPs in aquatic ecosystems. We improve the accuracy and quality of existing microplastics quantification methods by using depth-from-focus techniques to create 3D models of MPs.

Additionally, accurate 3D models of MPs can give insight into specific effects of MPs on ecosystems. For example, Ward et al. [23] find that "the extent of MP transport and deposition varied significantly by shape". Furthermore, they even find that "accurately modelling the shape of ... microplastic ... is crucial to determining the range and amount of [microplastic] deposition globally". The

shape of MPs is also significant in biological processes: according to Han et al. [10], "Nonspherical particles ... cylindrical polymer brushes ... and wirelike objects ... each [have] a unique influence on the cell".

1.2 Related Work

Microplastic Quantification Most forms of MP quantification are done by counting the number of MPs [13]. However, this methodology is actually ineffective in accurately quantifying MP concentrations. For example, MPs that are more prone to breakdown [22] may be mistakenly identified as being more prevalent. This could lead to ineffective policy and mitigation efforts, as true sources of MP pollution are not properly dealt with. Thus, measures like volume (which can be measured through 3D analysis) are necessary for a more accurate and effective assessment of MP pollution.

Raman Spectroscopy Raman spectroscopy [2] is based on the scattering of light, where a small fraction of the light interacts with the molecular vibrations of the sample, causing a shift in the energy of the scattered light. This shift, known as the Raman shift, provides a distinct spectrum that can be used to identify physical and chemical properties of the given substance. Although Raman spectroscopy is a popular technique in MP research, Raman spectrometers are expensive and require specialist knowledge to operate. Our automated approach thus offers a viable alternative with improved accessibility.

Mathematical Model Barchiesi et al. [3] propose a model to estimate surface area and volume from 2D images: the model assumes a best-fit ellipse to estimate the volume of MPs. Given the major axis (M) and minor axis (m) of the best fit ellipse, Barchiesi et al formulate the estimated volume as

$$V_{\text{Barchiesi}} = C_f \times \frac{4}{3} \times \pi \times \left(\frac{M}{2}\right)\left(\frac{m}{2}\right)\left(\left(\frac{m}{M}\right)_{\text{median}} \times \left(\frac{m}{2}\right)\right) \tag{1}$$

where C_f is a proposed measure to account for surface irregularity. We believe the proposed model is insufficiently expressive to be accurate: given the wide variety of MP morphologies (e.g. fragment, fiber and bead), the assumption that a best fit ellipse is appropriate is unfounded. Thus, predictions made by the model cannot be effectively used to quantify the MP pollution or qualify environmental effects of individual MPs.

2 Methodology

Our methodology consists of two main phases: classification and 3D reconstruction. To collect the data necessary for inference, we built a microscope with an electronically actuated focus mechanism (Figure 1). We designed a custom toothed translation screw to convert the rotary motion of the 12V stepper motor

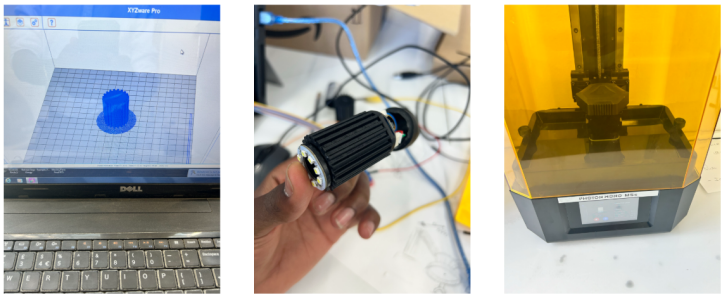

Fig. 1: Images taken during the development of the focus-actuation system

to linear motion of the objective lens. This component was created via resin 3D printing. The motor is controlled by an Arduino UNO, running the power input through a 12V relay. The total cost of our components is around 40 USD, which is substantially lower than that of research grade microscopes with similar characteristics. Considering available options, we found that similar research-grade microscopes with comparable magnification levels and an HDMI camera typically cost around 2500 USD [1, 12, 17].

2.1 Segmentation

To accurately reconstruct of objects within the scenes, the objects must first be identified. This is done with methodology proposed by Felzenszwalb et al. in "Efficient Graph-Based Image Segmentation" (EGBIS) [8]. EGBIS represents the image as a graph $G = (V, E)$, where each node $v_i \in V$ represents a pixel and each edge $(v_i, v_j) \in E$ represents similarity between pixels v_i and v_j.

The benefits of this algorithm over alternatives (e.g. YOLO [19] and CNN-based region proposal networks [20]) are twofold.

EGBIS is significantly more efficient than YOLO and CNN-based region proposal networks (RPN). The unparameterised segmentation algorithm runs in $O(mlogm)$ time and runs in a fraction of a second for the 640x480 images taken by the microscope camera. YOLO and CNN-based RPNs are significantly less efficient in our application: this is as the collection of images is staggered, which means optimisations of the

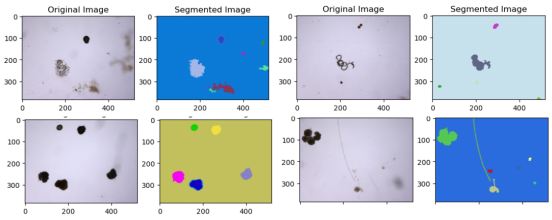

Fig. 2: Example images segmented with the EGBIS algorithm. The algorithm is clearly able to identify objects in the image, regardless of the irregular structure (e.g. the fibrous structure in the bottom right image)

algorithm for GPUs are not used.

EGBIS is much more accurate than neural-network-based approaches. YOLO [19] and CNN-based RPNs [20] are trained on data that do not contain microscopy images. This means that the models are often unable to identify objects in the scene, likely as colors and structures encountered will be unfamiliar. The EGBIS algorithm does not take semantic information into account, and is thus able to identify objects despite their irregular geometries. The uniform background colour and distinct separation between adjacent particles further improve the performance of the algorithm.

We perform segmentation on the model $\mathbf{M} = R(\mathbf{I}_f, k)$. The function $R(\mathbf{x}, k)$ denotes the EGBIS algorithm given the focus-stacked image $\mathbf{I}_f$ and parameter k. k parameterises the scale of objects preferred within the final segmentation (i.e. a large k will result in larger segmented objects and a smaller k will result in smaller segmented objects). The segmentation mask $\mathbf{M}$ (as seen in Figure 2) is defined as such: the entry $\mathbf{M}_{i,j}$ denotes the object that the pixel $\mathbf{I}_f(i, j)$ is a part of. It therefore takes a value between 1 and n, where n is the number of objects.

3 Classification

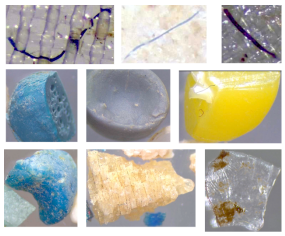

Fig. 3: Microplastic images from the ASU dataset

During the classification stage, our goal is to distinguish microplastics from a mixed sample containing both microplastics and non-microplastics, and to accurately classify the identified microplastics according to their morphology. Due to the limited availability of light-microscopy microplastic data, we must use few-shot learning. For our purposes, we employ a prototypical network-based methodology [21]. As proposed by Snell et al., we learn a mapping $f(x)$ from a given input image $\mathbf{x}_i$ to a point $\mathbf{c_k} \in \mathbb{R}$ in embedding space. We learn the parameters of $f(x)$ by minimising the loss function.

$$\mathcal{L} = \sum_{(\mathbf{x}_q, y_q) \in Q} \left\| f(\mathbf{x}_q) - \mathbf{c}_{y_q} \right\|^2 \tag{2}$$

where $(\mathbf{x}_q, y_q)$ is an input-label pair within the query set (the images that we aim to classify) and $\mathbf{c}_{y_q}$ is the corresponding prototype for class y_q.

We initialise our mapping $f(\mathbf{x})$ with a pretrained deep residual network [11] trained on the ImageNet dataset. We then convert the model to a mapping by replacing the final classification layer with a 256-node dense layer. Therefore, the output of the model will be the mapped point in embedding space $f(\mathbf{x}) \in \mathbb{R}^{256}$.

We fine-tune the model on the ASU MP dataset [6] (Figure 3), images from the IDR database [24]. To increase the size of the dataset we augment the data by performing random blurring and flipping of the images. This is well motivated

as the classification of a MP should be invariant to the focus and orientation of the image.

3.1 3D Reconstruction

From classification, we identify the regions where a MP is present within the image. With this information, we can then continue to construct a 3D model of individual MPs. To achieve this, we employ the depth-from-focus method.

We attempted both stereo depth estimation and monocular depth estimation but found that both methods were inadequate. For stereo depth estimation, the restrictively small field of view of MPs makes recording images with significant parallax difficult. Similarly, monocular depth estimation is speculative when generating depth maps and is often unable to recover fine details of the object.

Extracting depth information from depth-from-focus (DFF) is significantly less popular than other means due to "low precision hardware" and "imprecise mathematical methods" [25]. To make DFF an appropriate methodology for this purpose, we fix both of these limitations.

On the hardware front, our implemented solution can perform precise changes in magnification. Coupled with effective calibration, our hardware is far more effective than those used in previous implementations of DFF-based depth estimation. On the software front, we employ state-of-the-art research on blur detection to effectively extract fine details of the MPs. Specifically, we utilise Golestaneh et al.'s methodology [9] for applying blur detection on the images captured by the microscope. This is far more effective than using traditional methods (e.g. Laplacian-based methodologies) as fine details are preserved.

We set up a camera with real coordinates $\mathbf{C}$ (taking the centre of the sample as $(0, 0, 0)$) and take images with incrementing magnification and automatically disqualify images with excessively high blurriness. We also record sensor position s (the distance of the DSLR sensor from the objective lens) for each image.

For each of the images, we generate a focus map (Figure 4) $\mathbf{F}$, where $\mathbf{F}_{i,j}$ represents the focus of the pixel at (i, j). We aim to combine the focus maps generated to obtain a depth map $\mathbf{D}$ for which the entry at $\mathbf{D}_{i,j}$ denotes the distance along the ray connecting the sample and the camera $\mathbf{C}$.

The first step of this process involves aligning each of the generated focus maps, such that the focus maps can be overlaid to create a cohesive depth map. This is done using the SIFT methodology [16]. Suppose we wish to align $\mathbf{F}_1$ (the focus map corresponding to $\mathbf{I}_1$) to $\mathbf{F}_2$ (the focus map corresponding to $\mathbf{I}_2$): we first generate two sets of keypoints ($\mathbf{k}_1$ and $\mathbf{k}_2$) from images $\mathbf{I}_1$ and $\mathbf{I}_2$ using the SIFT methodology.

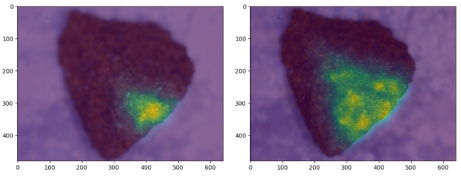

Fig. 4: Example of generated focus maps of the same object at different magnifications.

We then use a FLANN (Fast Library for Approximate Nearest Neighbors) [18] based matcher to find neighbors in $\mathbf{k}_2$ for keypoints in $\mathbf{k}_1$. We can then estimate a homography matrix $\mathbf{H}$ which best describes the mapping of the keypoints. By applying the homography matrix $\mathbf{H}$ on $\mathbf{F_1}$, we can align depth map $\mathbf{F_2}$ to $\mathbf{F}_2$. In practice, this process is highly accurate. This is as zooming and camera and movement are very slight, making the nearest neighbor identification very accurate.

We then use this information to calculate the desired depth map $\mathbf{D}$. Using the thin-lens formula, we can trivially determine the depth of each point:

$$\mathbf{D}_{i,j} = \frac{s^* f}{s^* - f} \tag{3}$$

where f is the focal length of the camera and s^* is the sensor position that achieves maximal focus. We merge the points for different camera positions and apply Delaunay triangulation [14] to create a mesh of the microplastic.

4 Results

Example meshes (Figure 5b) were generated from MPs (Figure 5c) found during manual sample collection at the River Itchen. Negative data (i.e. microscopy images of non-MPs) included images sourced from the IDR database and manually collected samples from the River Itchen.

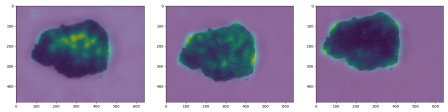

(a) Generated focus maps of a microplastic

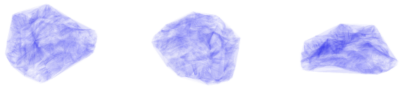

(b) Generated mesh from a microplastic

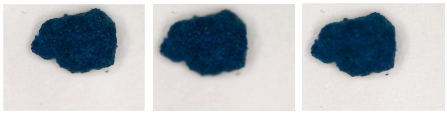

(c) Source images of a microplastic

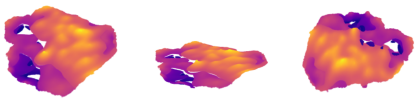

(d) Contour generated from depth

5 Discussion

As stated previously, the data used for model fine-tuning consists of light microscopy images [6] of MPs of different morphologies (60 images of bead MPs, 120 images of fiber MPs and 84 images of fragment MPs) and a negative dataset constructed from IDR [24] data. This data includes both images obtained from performing data augmentation and images originally from the dataset. 5 random IDR light microscopy datasets were selected to construct the negative dataset.

Method	Feature Dim	Classify (%)	Identify (%)	FP (%)	FN(%)
Baseline	128	53.4	35.7	33.9	30.4
Trained	128	62.3	40.6	26.5	32.9
Baseline	256	91.0	91.9	5.4	2.7
Trained	256	**94.6**	**96.3**	**2.4**	**1.3**
Baseline	512	87.4	89.8	5.7	5.5
Trained	512	93.2	90.1	6.3	3.6

Table 1: Performance of the classification model. FP and FN are abbreviations of false positive and false negative rates for the identification of MPs. Feature Dim refers to the output dimension of the feature extractor.

For every image in the dataset, the EGBIS algorithm was used to construct bounding boxes for each object within the image which were then used to save images that contain the negative object. We then randomly selected 100 images such as to reduce class imbalance during training.

Within Table 1, "Baseline" refers to results obtained using the few-shot learning model with the pretrained feature extractor and "Trained" refers to results obtained using the few-shot learning model after fine-tuning on the dataset. Identification accuracy refers to the accuracy of the model in separating MPs from non-MPs in unseen images. Within this testing paradigm, classifying a MP as the wrong morphology would still be considered correctly classified instance. Classification accuracy refers to the accuracy of identifying the morphology of the MP in an unseen image. Negative images are not included during the evaluation of classification accuracy. Training of the model is done on 60% of the dataset, evaluation on 10% and testing on 30%.

The classification model achieves highest accuracy (94.6% accuracy for MP classification, 96.3% accuracy on identification) when using a feature extractor with 256-dimensional output vectors. With 512-dimensional and 128-dimensional feature vectors, the accuracy decreases. There is likely not enough data for the feature extractor with 512-dimensional feature vectors to converge and the generated 128-dimensional feature vectors will not contain enough information to allow for accurate classification.

For MP identification, False positive rates seem consistently higher than false negative (Table 1): this is likely due to class imbalance within the dataset as well as similar characteristics between non-MPs and MPs particles.

The mesh generated by the model accurately reconstructs features of the MP. For example, the distinctive ridge of the MP is preserved, as well as the angularity of its structure. However, through the Delaunay triangulation performed to generate the mesh, some of the structural information is lost. Nevertheless, we believe that the generated representation is significantly more accurate than that of existing mathematical models. This is as our methodology is more expressive than our models, as no restrictive assumptions about the MP are made.

Additionally, we were unable to perform 3D reconstruction of bead and fibre type MPs as we were unable to find any samples of bead and fibre MPs in the Itchen River.

6 Conclusion

Our work presents a novel computer-vision based approach to the understudied field of reconstructing models of MPs. Operating on low-cost hardware, we adapted existing algorithms to effectively extract information from low-resolution information. However, more work must be done to test reconstruction for other MP morphologies, as well as calibrate generated models to experimentally determined values. Additonally, we expect continued difficulty in verifying the validity of the reconstructed models in futrue works: this is as retrieving the ground truth structure data is a difficult and costly task. Collaboration with reseachers from fields such as radiography will be necessary to collect ground truth data for collected MPs.

References

1. AmScope: Amscope 40x-1000x plan infinity kohler laboratory research microscope with hdmi camera hd monitor (2024), https://microscopecentral.com/products/amscope-40x-1000x-plan-infinity-kohler-laboratory-research-microscope-with-hdmi-camera-hd-monitor, accessed: 2024-08-16
2. Araujo, C.F., Nolasco, M.M., Ribeiro, A.M., Ribeiro-Claro, P.J.: Identification of microplastics using Raman spectroscopy: Latest developments and future prospects. Water research **142**, 426–440 (10 2018). https://doi.org/10.1016/j.watres.2018.05.060, https://doi.org/10.1016/j.watres.2018.05.060
3. Barchiesi, M., Kooi, M., Koelmans, A.A.: Adding depth to microplastics. Environmental science technology **57**(37), 14015–14023 (9 2023). https://doi.org/10.1021/acs.est.3c03620, https://doi.org/10.1021/acs.est.3c03620
4. Bergami, E., Bocci, E., Vannuccini, M.L., Monopoli, M., Salvati, A., Dawson, K.A., Corsi, I.: Nano-sized polystyrene affects feeding, behavior and physiology of brine shrimp Artemia franciscana larvae. Ecotoxicology and environmental safety **123**, 18–25 (1 2016). https://doi.org/10.1016/j.ecoenv.2015.09.021, https://doi.org/10.1016/j.ecoenv.2015.09.021
5. Bergmann, M., Gutow, L., Klages, M.: Marine Anthropogenic litter (1 2015). https://doi.org/10.1007/978-3-319-16510-3, https://doi.org/10.1007/978-3-319-16510-3
6. for Data Science, U.: Microplastics image dataset (2021), https://github.com/UnitForDataScience/Microplastics_Image_Dataset, accessed: 2024-06-25
7. Eriksen, M., Cowger, W., Erdle, L.M., Coffin, S., Villarrubia-Gómez, P., Moore, C.J., Carpenter, E.J., Day, R.H., Thiel, M., Wilcox, C.: A growing plastic smog, now estimated to be over 170 trillion plastic particles afloat in the world's oceans—Urgent solutions required. PloS one **18**(3), e0281596 (3 2023). https://doi.org/10.1371/journal.pone.0281596, https://doi.org/10.1371/journal.pone.0281596

8. Felzenszwalb, P.F., Huttenlocher, D.P.: Efficient Graph-Based image segmentation. International journal of computer vision **59**(2), 167–181 (9 2004). https://doi.org/10.1023/b:visi.0000022288.19776.77, https://doi.org/10.1023/b:visi.0000022288.19776.77
9. Golestaneh, S.A., Karam, L.J.: Spatially-Varying Blur Detection Based on Multiscale Fused and Sorted Transform Coefficients of Gradient Magnitudes. CVPR (7 2017). https://doi.org/10.1109/cvpr.2017.71, https://doi.org/10.1109/cvpr.2017.71
10. Han, S., Bang, J., Choi, D., Hwang, J., Kim, T., Oh, Y., Hwang, Y., Choi, J., Hong, J.: Surface pattern analysis of microplastics and their impact on Human-Derived cells. ACS applied polymer materials **2**(11), 4541–4550 (8 2020). https://doi.org/10.1021/acsapm.0c00645, https://doi.org/10.1021/acsapm.0c00645
11. He, K., Zhang, X., Ren, S., Sun, J.: Deep Residual Learning for Image Recognition. CVPR 2016 (6 2016). https://doi.org/10.1109/cvpr.2016.90, https://doi.org/10.1109/cvpr.2016.90
12. Instruments, N.O..S.: National bti1-213-led led microscope with detachable tablet (2024), https://microscopecentral.com/products/national-bti1-213-led-led-microscope-with-detachable-tablet, accessed: 2024-08-16
13. Koelmans, A.A., Nor, N.H.M., Hermsen, E., Kooi, M., Mintenig, S.M., De France, J.: Microplastics in freshwaters and drinking water: Critical review and assessment of data quality. Water research **155**, 410–422 (5 2019). https://doi.org/10.1016/j.watres.2019.02.054, https://doi.org/10.1016/j.watres.2019.02.054
14. Lawson, C.L.: Transforming triangulations. Discrete mathematics **3**(4), 365–372 (1 1972). https://doi.org/10.1016/0012-365x(72)90093-3, https://doi.org/10.1016/0012-365x(72)90093-3
15. Lee, Y., Cho, J., Sohn, J., Kim, C.: Health effects of microplastic exposures: current issues and perspectives in South Korea. Yonsei Medical Journal/Yonsei medical journal **64**(5), 301 (1 2023). https://doi.org/10.3349/ymj.2023.0048, https://doi.org/10.3349/ymj.2023.0048
16. Lindeberg, T.: Scale invariant feature transform. Scholarpedia journal **7**(5), 10491 (1 2012). https://doi.org/10.4249/scholarpedia.10491, https://doi.org/10.4249/scholarpedia.10491
17. Microsystems, L.: Leica dm1000 high definition digital microscope (2024), https://microscopecentral.com/products/leica-dm1000-high-definition-digital-microscope, accessed: 2024-08-16
18. Muja, M., Lowe, D.G.: Scalable nearest neighbor algorithms for high dimensional data. IEEE transactions on pattern analysis and machine intelligence **36**(11), 2227–2240 (11 2014). https://doi.org/10.1109/tpami.2014.2321376, https://doi.org/10.1109/tpami.2014.2321376
19. Redmon, J., Divvala, S., Girshick, R., Farhadi, A.: You Only Look Once: Unified, Real-Time Object Detection (6 2016). https://doi.org/10.1109/cvpr.2016.91, https://doi.org/10.1109/cvpr.2016.91
20. Ren, S., He, K., Girshick, R., Sun, J.: Faster R-CNN: Towards Real-Time Object Detection with Region Proposal Networks. IEEE transactions on pattern analysis and machine intelligence **39**(6), 1137–1149 (6 2017). https://doi.org/10.1109/tpami.2016.2577031, https://doi.org/10.1109/tpami.2016.2577031
21. Ren, S., He, K., Girshick, R., Sun, J.: Prototypical networks for few-shot learning. Conference on Neural Information Processing Systems 2017 (2017), https://arxiv.org/abs/1703.05175

22. Sipe, J.M., Bossa, N., Berger, W., Von Windheim, N., Gall, K., Wiesner, M.R.: From bottle to microplastics: Can we estimate how our plastic products are breaking down? Science of the total environment **814**, 152460 (3 2022). https://doi.org/10.1016/j.scitotenv.2021.152460, https://doi.org/10.1016/j.scitotenv.2021.152460
23. Ward, E., Gordon, M., Hanson, R., Jantunen, L.M.: Modelling the effect of shape on atmospheric microplastic transport. Atmospheric environment p. 120458 (3 2024). https://doi.org/10.1016/j.atmosenv.2024.120458, https://doi.org/10.1016/j.atmosenv.2024.120458
24. Williams, E., Moore, J., Li, S.W., Rustici, G., Tarkowska, A., Chessel, A., Leo, S., Antal, B., Ferguson, R.K., Sarkans, U., Brazma, A., Salas, R.E.C., Swedlow, J.R.: Image Data Resource: a bioimage data integration and publication platform. Nature methods **14**(8), 775–781 (6 2017). https://doi.org/10.1038/nmeth.4326, https://doi.org/10.1038/nmeth.4326
25. Xiong, Y., Shafer, S.: Depth from focusing and defocusing. CVPR (12 2002). https://doi.org/10.1109/cvpr.1993.340977, https://doi.org/10.1109/cvpr.1993.340977